Iranian Journal of Medical Physics

ijmp.mums.ac.ir

Comparison of Methods of µ-Map Generation: MR-Based Method in PET/MR Imaging Versus Pseudo-CT Method in Radiotherapy Dose Planning

Isaac Kwesi Acquah[1,2*], Stephen Inkoom[2,3], Francis Hasford[2,3]

1. University of Education, Winneba, Ghana
2. University of Ghana, School of Nuclear and Allied Health Science, Ghana
3. Ghana Atomic Energy Commission, Ghana

ARTICLE INFO

Article type:
Original Paper

Article history:
Received: Jan 30, 2024
Accepted: May 12, 2024

Keywords:
Magnetic Resonance Imaging (MRI)
Computed Tomography (CT)
Positron-Emission tomography (PET)
Radiotherapy

ABSTRACT

Introduction: Attenuation correction is essential for accurate PET imaging and radiotherapy (RT) dose planning. However, PET/MR systems face a significant challenge due to the lack of direct attenuation data from MR images, unlike PET/CT where CT provides inherent attenuation information. Similarly, the increasing use of MRI in RT planning necessitates pseudo-CT methods for accurate dose calculation. This study compares MR-based µ-map generation for PET/MR and pseudo-CT methods for RT planning, addressing their challenges and limitations to improve treatment accuracy and patient care.

Material and Methods: The study involved patient selection, image processing, and generation of MR-based attenuation maps (µ-maps) for PET attenuation correction and pseudo-CTs for RT dose planning using advanced computational software.

Results: MR-based µ-maps, potentially useful for PET attenuation correction, and pseudo CTs, potentially applicable in radiotherapy planning, were successfully generated. Head images showed MR-based µ-maps overestimating bone for two patients (deviations of 4.0% and 4.2%). Both MR-based and CT µ-maps exhibited dynamic and continuous µ-values for head bone. In the pelvis, pseudo-CT underestimated bone volume in five patients (deviations of 18.7%, 21.3%, 9.6%, 14%, and 10%). Pseudo-CT's bone µ-values lacked continuity compared to CT µ-maps. Pelvis studies revealed more dynamic and broader µ-value range for muscle in CT µ-maps than pseudo-CT and MRI µ-map.

Conclusion: These findings suggest the need for careful consideration and validation of attenuation correction methods, especially in regions with complex anatomical structures, to ensure accurate treatment delivery and enhance patient care in the context of PET/MR and radiotherapy.

►*Please cite this article as:*
Acquah IK, Inkoom S, Hasford F. Comparison of Methods of µ-Map Generation: MR-Based Method in PET/MR Imaging Versus Pseudo-CT Method in Radiotherapy Dose Planning. Iran J Med Phys 2024; 21: 355-364. 10.22038/ijmp.2024.77457.2369.

Introduction

Positron emission tomography and magnetic resonance imaging (PET/MRI) is a hybrid imaging system that combines multi-parametric imaging capabilities to capture morphological, functional, and molecular data from the body [1]. This combination enables the simultaneous acquisition of high-resolution morphological, functional, and molecular data, providing a comprehensive assessment of physiological and pathological processes within the body [2]. PET/MRI is particularly advantageous in oncology, neurology, and cardiology, where precise localization and characterization of lesions are critical for diagnosis, treatment planning, and monitoring [3].

Positron Emission Tomography (PET) is a highly sensitive, non-invasive metabolic imaging technique that traces physiological and pathophysiological processes at the molecular level [4]. It operates on the principles of nuclear imaging, utilizing radiotracers radioactively labeled molecules that participate in specific biological processes [5]. When these tracers decay, they emit positrons, which subsequently undergo annihilation upon interaction with electrons [6]. This process results in the emission of two gamma rays traveling in opposite directions (approximately 180 degrees apart), which are detected by a ring of scintillation detectors [7]. The electronic collimation mechanism enhances PET's sensitivity, making it superior to conventional nuclear imaging modalities such as Single Photon Emission Computed Tomography (SPECT) [8].

Despite its exceptional sensitivity in detecting metabolic changes, PET alone lacks anatomical detail, which is a significant limitation [9]. To overcome this, it is often combined with structural imaging techniques like MRI or Computed Tomography (CT) [10]. While PET/CT is more commonly used in clinical practice, PET/MRI offers superior soft tissue contrast, reduced radiation exposure, and advanced functional

*Corresponding Author: Email: ikacquah@uew.edu.gh

imaging capabilities, making it particularly beneficial for applications in neuroimaging, pediatric oncology, and musculoskeletal assessments [11]. By integrating the strengths of magnetic resonance imaging (MRI) such as superior soft tissue contrast, diffusion-weighted imaging, and dynamic contrast-enhanced imaging with the quantitative physiologic and metabolic information from PET, this system has advanced diagnostic and therapeutic applications [12]. An essential aspect of PET imaging and radiotherapy (RT) dose planning is the knowledge of photon attenuation coefficients of various body tissues, which is crucial for accurately modeling attenuation and dose distribution [13]. Traditionally, computed tomography (CT) has been the standard method for obtaining photon attenuation coefficients [14]. However, with the increasing adoption of PET/MRI systems, particularly in developed countries, CT-derived attenuation coefficient maps are not directly available in these hybrid modalities [15]. Similarly, the growing use of MRI in RT dose planning instead of CT necessitates alternative methods to estimate photon attenuation within the body [16]. MRI-based RT planning offers superior soft tissue contrast, making it advantageous in tumor delineation and treatment planning, especially in brain tumors, head and neck cancers, and prostate cancer [17]. However, the lack of direct attenuation information in MRI necessitates novel approaches to derive attenuation maps for both PET imaging and RT dose calculations [18].

Various approaches have been developed to address attenuation correction in PET/MRI and radiotherapy, including segmentation-based methods, atlas-based techniques, and voxel-based methods [19]. Attenuation, defined as the gradual reduction of energy in a beam as it passes through matter, occurs due to processes such as scattering or absorption [20]. For photon beams, attenuation mechanisms include coherent scattering, photoelectric effect, Compton scattering, pair production, triplet production, and photodisintegration [21]. In PET imaging, attenuation specifically refers to the loss of true coincidence events resulting from the scattering or absorption of annihilation photons before they reach the detectors [22]. This loss negatively impacts image quality, increasing noise, artifacts, and errors in quantification [23]. Additionally, attenuation effects tend to intensify with larger body sizes [24].

Historically, CT has been the preferred modality for attenuation correction in PET/CT imaging [25]. However, limitations in CT's ability to provide detailed soft tissue contrast have led to a preference for PET/MRI in scenarios where soft tissue imaging is critical [26]. MRI's superior tissue contrast enhances diagnostic accuracy and provides more detailed visualization of soft tissues and fat. While CT images rely on Hounsfield units (HU) to represent attenuation, translating these values to linear attenuation coefficients (μ) at 511 keV for PET or to the photon spectrum of linear accelerators (linacs) remains a challenge [26]. MRI, operating on entirely different physical principles from CT, lacks a direct relationship between its signal and photon attenuation coefficients [27]. Instead, MR-based attenuation correction methods involve segmenting tissues into predefined classes, such as soft tissue, fat, lung, and bone, followed by the assignment of corresponding HU values [28].

Differences in expertise and organizational structures often result in limited collaboration between medical physicists working on attenuation correction for PET/MRI and those focusing on MRI-only RT dose planning. This study aims to compare the methodologies and outcomes of MR-based and pseudo-CT μ-map generation for PET/MRI and radiotherapy applications, highlighting their similarities, differences, and respective challenges.

Materials and Methods

Data Analysis

The data analysis approach in the manuscript involved meticulous patient selection, utilizing data from seven patients, Standardized image acquisition using advanced MRI and CT scanners, including the Siemens Biograph mCT PET/CT scanner for CT images and the Biograph mMR PET/MR scanner for PET and MR images, and rigorous image processing utilizing sophisticated software tools. Key steps included the conversion of Hounsfield Unit (HU) values to PET Linear Attenuation Coefficients (LAC), pseudo-CT creation using machine learning technology, and MR μ-map generation for PET attenuation correction. Comparative analyses between CT-based μ-maps, MR-based μ-maps, and pseudo-CTs were conducted to assess bone and muscle volume estimation. This comprehensive approach ensured robustness and reliability in interpreting study outcomes, contributing to the validity of our findings. The image processing algorithm and parameter settings were carefully outlined to ensure transparency and reproducibility. Specifically, the image processing involved several steps conducted using a high-performance computing system. Initially, the acquired MRI and CT images were pre-processed to enhance image quality and standardize imaging parameters. This included noise reduction using the masking method to mask out the surrounding areas of the image, intensity normalization, and spatial registration to ensure accurate alignment between modalities. Subsequently, a custom image processing pipeline was implemented using MATLAB R2018b, Statistical Parametric Mapping (SPM), and Elastix version 4.7. The MATLAB environment facilitated custom script development for image modification, co-registration, and masking. SPM was utilized for advanced image analysis and statistical modeling, while Elastix was employed for deformable image registration to ensure precise spatial alignment between MRI and CT datasets. Parameter settings for each software tool

were meticulously configured based on established guidelines and previous studies to optimize performance and accuracy. Additionally, quality control measures were implemented throughout the image processing pipeline to identify and mitigate potential artifacts or inconsistencies. Overall, the detailed description of the image processing algorithm and parameter settings ensures methodological transparency and reproducibility, facilitating the validation and interpretation of the study results.

Eligibility Criteria

This study included two lung cancer and five lymphoma patients from St. Olavs Hospital, Trondheim, Norway. Head CT and MR images were used for lung cancer, while pelvis CT and MR images were used for lymphoma. The study began with lung cancer patients but expanded to include lymphoma patients due to the specific compatibility of the MRI planner software with pelvic MR images. Inclusion criteria required T2-weighted images, corresponding CT images, and coverage of the abdominal anatomical body region. Patients who did not meet these criteria were excluded.

Image Acquisition

Images for this study were sourced from St. Olav's Hospital in Trondheim, Norway, utilizing Siemens scanners installed in 2013: the Biograph mCT PET/CT scanner for CT images and the Biograph mMR PET/MR scanner for PET and MR images. Ultrashort echo sequence (UTE) was employed for head MR images to generate the μ-map. Patients with lung and lymphoma cancer underwent PET/CT and PET/MR examinations post fluorodeoxyglucose (FDG) injection, with informed consent. Head images from lung cancer patients used UTE and T2-weighted sequences, with a protocol including a repetition time (TR) of 11.94 ms, echo time (TE) of 0.07 ms, a field of view of 300 x 300 mm², a flip angle of 150°, a slice thickness of 3.0 mm, and 44 slices. Pelvis/abdomen images from lymphoma patients employed DIXON and T2-weighted sequences, with a protocol including a TR of 3.60 ms, TE of 1.23 ms, a field of view of 3288 x 500 mm², a flip angle of 150°, a slice thickness of 3.0 mm, and 31 slices.

Image Processing

The study used an HP Pavilion g6 with a 64-bit AMD A10-4600M CPU, 2.30 GHz clock speed, 8 GB RAM, and Windows 10 Pro for image processing. Radiant DICOM Viewer was used for viewing, and MATLAB R2018b, Statistical Parametric Mapping (SPM), and Elastix version 4.7 were used for image modification, co-registration, and image masking.

The Conversion of the Hounsfield Unit (HU) To PET Linear Attenuation Coefficients (LAC)

One of the primary challenges in using CT images for PET attenuation correction lies in converting Hounsfield unit (HU) values from CT images into linear attenuation coefficients (μ) at 511 keV and further adapting these to μ-values for the photon spectrum of the linear accelerator (linac) [29].

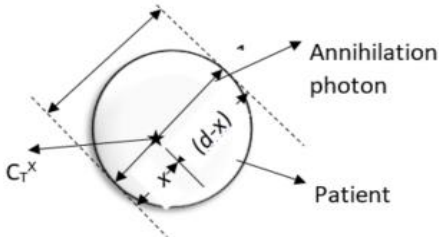

Figure 1. Illustration of the annihilation process within a patient's body.

As shown in Figure 1, the point of annihilation is represented by CT at position *x*, with the photon detection path having a total length *d*. One photon travels a distance *x*, while the other travels (d−x). For the images used in this study, a peak voltage of 120 kV was applied, with a breakpoint set at 47 HU. Specific *a* and *b* coefficients were utilized to account for the conversion. Following the methodology outlined in [26], the slopes were determined using Equations 1 and 2:

$$y_1 = [9.6 \times 10^{-5}(HU + 1000)\ cm^{-1} \quad (1)$$

$$y_2 = [a(HU + 1000) + b]\ cm^{-1} \quad (2)$$

Pseudo CT Creation

The MRI-planner (version 2.0), developed by Spectronic Medical in Sweden, was designed to promote the use of MRI-only radiotherapy, aiming to enhance tumor treatment while minimizing side effects [30]. This software, specifically for research purposes and not yet approved for clinical application, generates pseudo-CT images from standard MR images using a statistical decomposition algorithm. Built on the principles of the atlas-based method for attenuation correction, the MRI-planner employs advanced machine learning technology. The process involves uploading T2-weighted MR images to an online server, where the pseudo-CT images are generated within a few hours.

MR μ-Map Generation

The MR μ-map was generated using Siemens software (version VE11P) available at the PET Center of St. Olav Hospital, Trondheim, Norway. This software, integrated with the PET/MR machine and developed by Siemens, employs machine learning technology to generate μ-maps from MR images for PET attenuation correction. Notably, the software provides options to include bone in the μ-map when necessary. It has been operational since 2013.

CT at 511 KeV μ-Map Generation

For the creation of the head μ-map, three types of images were utilized: whole-body CT images, MR T2-weighted images, and the MR-based μ-map. The whole-body CT images were cropped to exclude regions below the neck. Regions of interest (ROIs) were defined on each slide, and the CT-HEAD images were masked to remove surrounding noise, resulting in the masked CT-

HEAD images. These masked images were then registered to the MR T2-weighted images using SPM and Elastix tools. Subsequently, the registered CT-HEAD and MR T2-weighted images were converted to 511 keV PET LAC using a bilinear conversion function based on the method described by.

Results

Conversion of Hounsfield Unit (HU) to PET Linear Attenuation Coefficient (LAC)

The conversion of Hounsfield Units (HU) to PET Linear Attenuation Coefficients (LAC) at 511 keV was performed using a bilinear method described by Carney, Townsend [26]. A MATLAB function was developed based on this relationship to transform the CT image volume with voxel values in HU into 511 keV LAC μ-maps. Figure 2 illustrates the original CT image in Hounsfield units and its corresponding 511 keV PET LAC image. After the conversion, the 511 keV PET LAC image displayed noticeably increased brightness compared to the original.

CT at 511 KeV μ-Map VS MR-Based μ-Map

The μ-map analysis involved various comparisons, starting with a qualitative assessment by visually comparing each CT slide at 511 keV μ-map with its corresponding MR-based μ-map slide. Visual inspection revealed that the MR-based μ-map generally overestimated bone in most regions compared to the CT μ-map, as highlighted in Figure 3. In some areas, however, bone was underestimated, as shown in Figures 4. Overall, bone overestimation was more prevalent in the MR-based μ-map than underestimation. These differences are highlighted with red circles in selected slides from patients 130 and 124 in Figures 3 and 5.

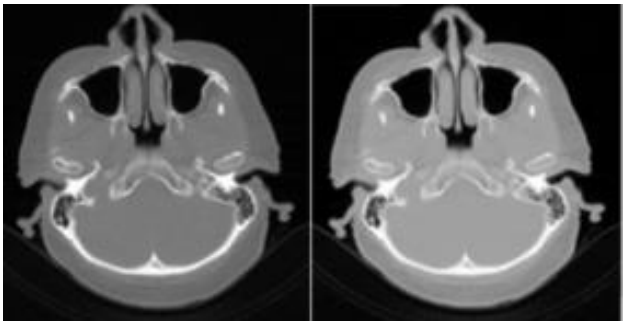

Figure 2. CT image with voxel values in Hounsfield units (left) and its conversion to 511 keV PET Linear Attenuation Coefficients (right)

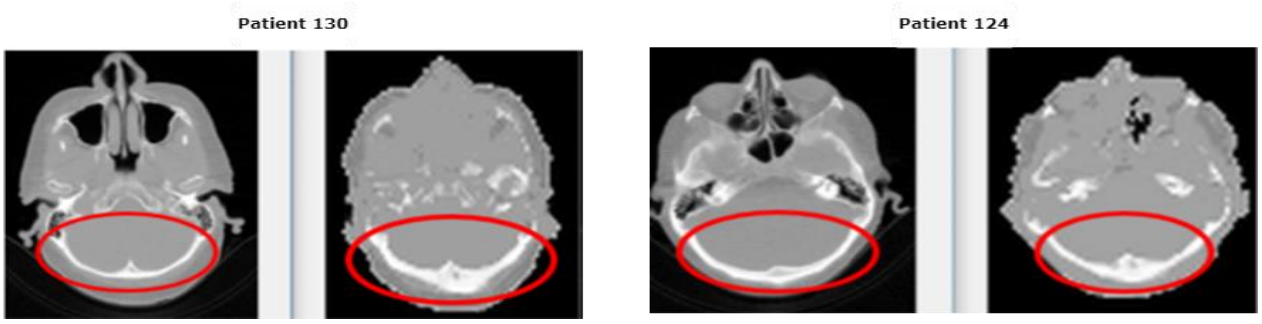

Figure 3. Slides showing bone overestimation in patient 130 and 124

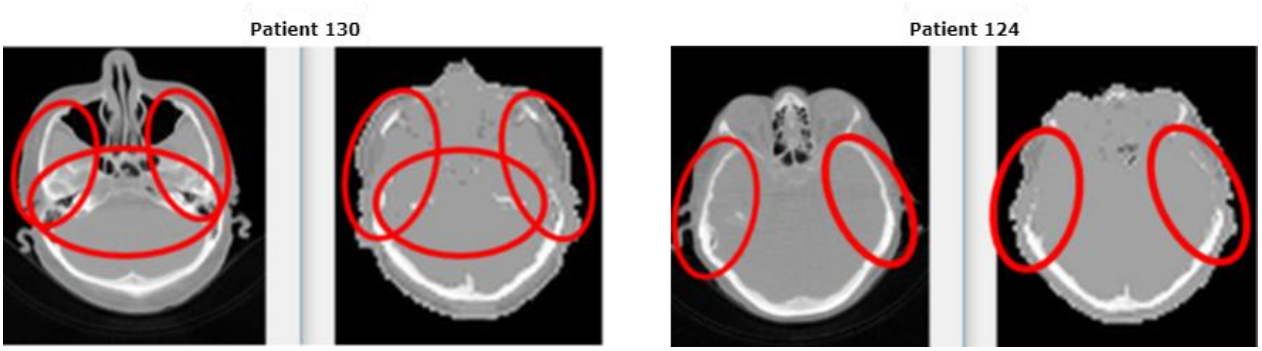

Figure 4. slides showing bone underestimation for patients 130 and 124

New Scatter Plots of CT at 511 keV μ-Values VS MR-Based μ-Values

To compare the CT at 511 keV μ-map with the MR-based μ-map, over 10,000 μ-values were plotted, revealing an approximately linear relationship between them, as shown in Figure 5. This indicates that most points in the CT μ-map had corresponding values in the MR-based μ-map. The findings suggest that the MR-based μ-map can serve as a viable alternative for attenuation correction when the CT μ-map at 511 keV is unavailable.

Bone Volume Plots

For both patients (130 and 124), the MR-based μ-map showed a larger bone volume compared to the CT μ-map. For Patient 130, the bone volumes were 2357 cm³ for the CT μ-map and 2456 cm³ for the MR-based μ-map, with a difference of 99 cm³, representing a 4.04% increase as shown in Figure 6. Similarly, for Patient 124, the bone volumes were 2254 cm³ for the CT μ-map and 2345 cm³ for the MR-based μ-map, with a difference of 91 cm³, also indicating a 4.04% increase as shown in Figure 6.

Box Plot of μ-Values in the Bone Volume

In this study, the variation in the μ-values of bone within the bone volume was analyzed using MATLAB. A custom script was used to generate box plots for the comparison. For Patient 130, 271,911 μ-values were plotted, with median μ-values of 0.1396 cm^{-1} and 0.1468 cm^{-1} for the CT μ-map and MR-based μ-map, respectively. As shown in Figure 7, there was minimal variation in μ-values between the two maps, with a finite number of outliers estimated at 410 for the CT μ-map and 135 for the MR-based μ-map. Similarly, for patient 124, 300,000 μ-values were plotted, with median μ-values of 0.1460 cm^{-1} and 0.1461 cm^{-1} for the CT μ-map and MR-based μ-map, respectively. Figure 7 also demonstrates minimal variation in μ-values between the maps, with outliers estimated at 104 for the CT μ-map and 264 for the MR-based μ-map.

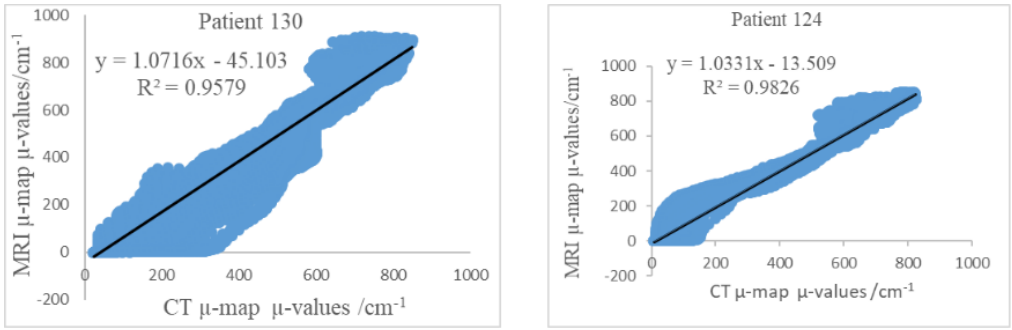

Figure 5. Scatter plots showing CT at 511 keV μ-values versus MR-based μ-values for Patient 130 and 124

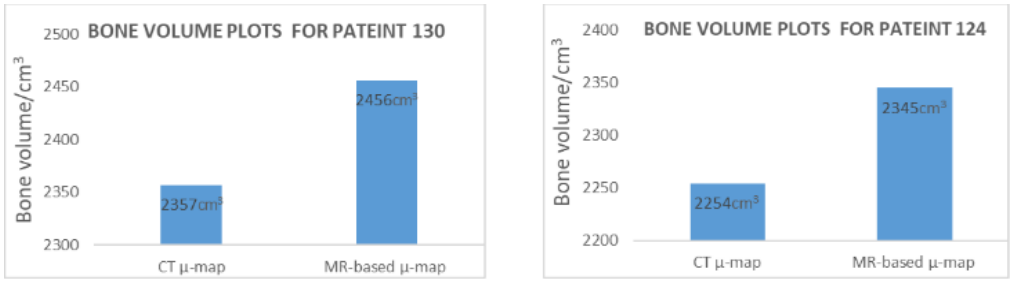

Figure 6. Comparison of the bone volume of CT μ map and MR-based μ map for patient 130 and 124

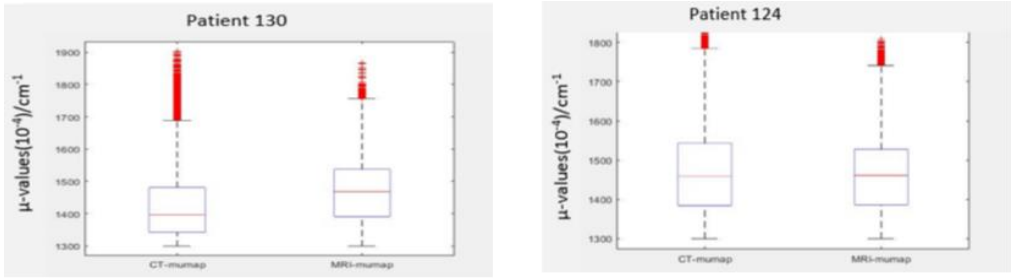

Figure 7. Box plot illustrating the variation in μ-values within the bone volume for Patient 130 and 124

Results from Pelvis Studies

The Conversion of HU to PET LAC

A scale factor of 10^4 was applied to the LAC to enhance the linear attenuation values for easier comparison. As shown in Figure 8, the conversion resulted in a noticeable increase in brightness in the image.

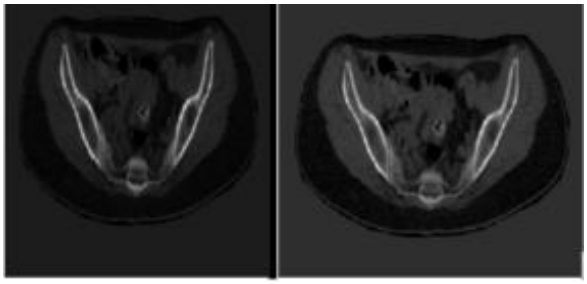

Figure 8. Slides showing before and after conversion of HU to PET Linear Attenuation Coefficients

Comparison between CT- μ-MAP, MRI- μ-MAP, and Pseudo-CT for Bone

This study utilized Matlab to analyze bone volume in abdominal images across three μ-maps, specifically focusing on comparing CT-μ-map and pseudo-CT volumes at 511 keV. The investigation involved patients from 1 to 5, each presenting distinctive findings. For Patient 1, the CT-μ-map displayed a bone volume of 850 cm³, whereas the pseudo-CT showed 691 cm³, indicating an 18.7% decrease. In the case of Patient 2, the CT-μ-map exhibited a bone volume of 1200 cm³, while the pseudo-CT volume was 945 cm³, reflecting a 21.3% decrease. Patient 3 demonstrated bone volumes of 721 cm³ for the CT-μ-map and 652 cm³ for the pseudo-CT, resulting in a 9.6% decrease. For Patient 4, the CT-μ-map recorded a bone volume of 945 cm³, whereas the pseudo-CT displayed 812 cm³, indicating a 14% decrease. Patient 5 showcased CT-μ-map and pseudo-CT bone volumes of 1023 cm³ and 921 cm³, respectively, representing a 10% decrease. In all cases, the CT-μ-map, considered the gold standard, consistently demonstrated higher bone volumes compared to the pseudo-CT. The graphical representations in Figure 9 emphasize the observed trends, underscoring the pseudo-CT's consistent tendency to underestimate bone volume across the analyzed images.

It was noted that the pseudo-CT exhibited limited variability, and there was minimal fluctuation in the μ-values. This indicates that the MRI-planner software was still in its early stages of development, with ongoing efforts by developers to enhance its variability and achieve more consistent μ-values. In the abdominal part of the study, 9000 random bone μ-values were plotted for the five analyzed images. For patient 1, median μ-values were 0.1725 cm^{-1} and 0.1727 cm^{-1} for CT μ-map and pseudo-CT, with finite outliers of 215 and 759 observed for CT μ-map and pseudo-CT, respectively. Similar patterns were observed for patients 2 to 5. Figure 10 highlight substantial variation in μ-values, emphasizing the greater variability and continuous values of the CT μ-map compared to the less varying and discontinuous nature of the pseudo-CT, which exhibited finite outliers of 215 and 759 for CT μ-map and pseudo-CT, respectively.

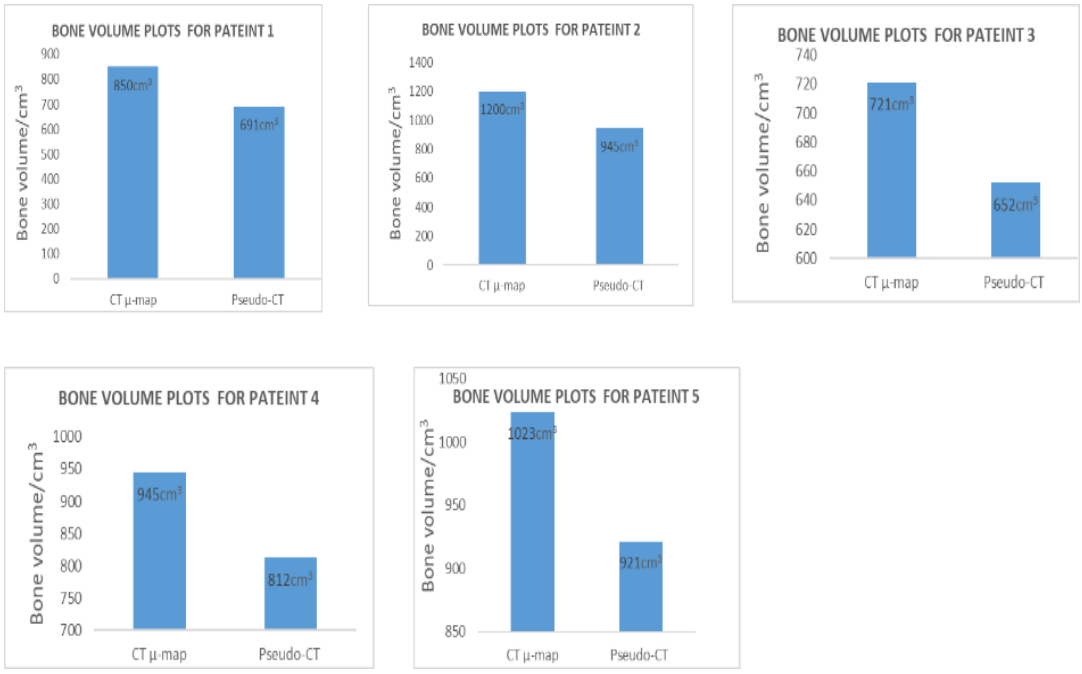

Figure 9. Comparison of the bone volume of CT μ-map and pseudo-CT for patient 1,2,3,4 and 5.

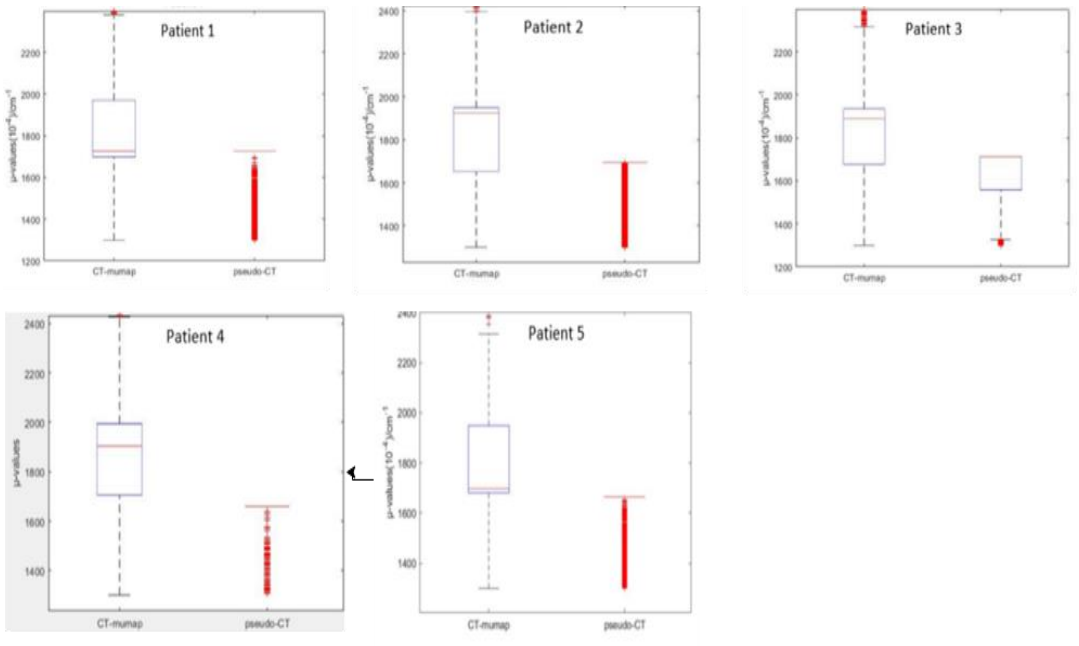

Figure 10. Variation in μ-values for bone-in CT μ-map and pseudo-CT for patient 1,2,3,4 and 5

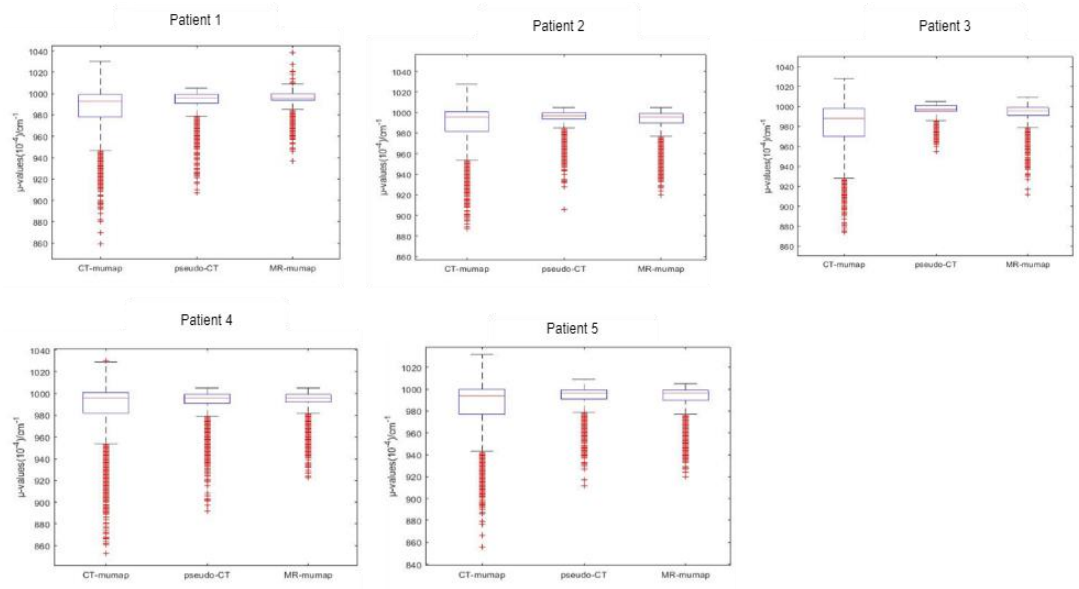

Figure 11. μ-values for muscle in CT- μ-map, pseudo-CT, and MR μ-map for patient 1,2,3,4 and 5

Comparison Between the CT- μ-MAP, MRI- μ-MAP, and Pseudo CT for Muscle

For patient 1, the average muscle μ-values were 0.0995 cm^{-1}, 0.0992 cm^{-1}, and 0.0995 cm^{-1} for CT μ-map, Pseudo-CT, and MR μ-map, respectively. In the plotted μ-values, there were 262, 467, and 376 outliers for CT μ-map, Pseudo-CT, and MR μ-map, respectively, as depicted in figure 11. Similarly, for patient 2, the mean muscle μ-values were 0.0989 cm^{-1}, 0.0997 cm^{-1}, and 0.0994 cm^{-1} for CT μ-map, Pseudo-CT, and MR μ-map, with 425, 487, and 840 outliers in the respective maps shown in figure 11. This pattern continued for patients 3 to 5, where the mean muscle μ-values for CT μ-map, Pseudo-CT, and MR μ-map were accompanied by outliers in figures 11. Generally, it was observed that muscle μ-values varied across all maps but were more varying and had a broader range in the CT μ-map compared to Pseudo-CT and MR μ-map.

Discussion

The study compares methods of μ-map generation in PET/MR imaging and radiotherapy dose planning, focusing on MR-based and pseudo-CT μ-map generation. It reveals several significant findings with implications for both imaging accuracy and treatment planning.

In comparison to CT-based μ-maps, the study finds that MR-based μ-maps tend to overestimate bone volume, particularly evident in head images. This observation aligns with previous research highlighting differences in tissue characterization between MR and CT imaging modalities.

A 2022 review Florkow, Willemsen [31] highlighted that MRI is increasingly utilized as a radiation-free alternative to CT for diagnosing and planning treatment of musculoskeletal pathologies. Despite challenges in imaging cortical bone due to low proton density, recent developments in MR image acquisition and processing have enhanced bone contrast on MR images, making MRI a viable option in certain clinical scenarios. The linear relationship observed between μ-values in MR-based and CT-based μ-maps suggests the potential viability of MR-based μ-maps for attenuation correction, supporting findings from previous studies. A study from [32] discusses the integration of anatomical imaging modalities like CT and MRI with PET and SPECT. It emphasizes that while CT provides direct attenuation information, MRI's superior soft tissue contrast can be leveraged to develop attenuation correction methods, suggesting the feasibility of MR-based μ-maps in clinical practice.

However, the study also notes consistent underestimation of bone volume in pseudo-CT compared to CT-μ-maps in the pelvis region. This discrepancy underscores the need for further refinement of pseudo-CT generation methods to improve accuracy, a challenge acknowledged in prior research. The limited variability and fewer outliers observed in pseudo-CT μ-values compared to CT-based μ-maps emphasize ongoing development efforts needed to enhance pseudo-CT variability and achieve more consistent μ-values, a goal echoed in the literature. Discrepancies in μ-map generation between MR-based and pseudo-CT methods could lead to inaccuracies in dose calculation and delivery during radiotherapy, potentially affecting treatment efficacy and toxicity. These discrepancies may also impact PET image reconstruction accuracy, influencing lesion detection and characterization in PET/MR imaging. Analysis of muscle tissue μ-values reveals variation across all maps, with CT-μ-maps exhibiting a broader range compared to pseudo-CT and MR-based μ-maps. This variation highlights the importance of accurately characterizing different tissue types for both PET attenuation correction and radiotherapy planning, an aspect recognized in previous investigations.

The study highlights challenges in μ-map generation for PET/MR imaging and radiotherapy dose planning, emphasizing the need for validation of attenuation correction methods in complex anatomical regions.

The study's limitations encompass various aspects, including sample size, anatomical focus, computational methods, and clinical implications. With a small sample size limited to specific cancer types and anatomical regions, the findings may not fully represent diverse patient populations. Technical challenges associated with image processing algorithms and software packages could introduce biases and uncertainties, particularly in pseudo-CT generation. Furthermore, the study lacks long-term clinical data to evaluate the real-world impact of μ-map generation methods on treatment outcomes. These limitations underscore the need for larger, more diverse studies with rigorous validation and long-term follow-up to ensure the reliability and generalizability of results in clinical practice.

Conclusion

In conclusion, this study explored the comparison between MR-based and pseudo CT μ-map generation for attenuation correction in PET/MR and radiotherapy planning, respectively. The results indicate successful generation of both MR-based μ-maps for PET and pseudo CTs for radiotherapy dose planning. However, notable discrepancies were observed in bone estimation for head images, where MR-based μ-maps tended to overestimate bone compared to CT μ-maps. Additionally, pseudo-CTs for pelvis planning underestimated bone volume and exhibited less dynamic μ-values for both bone and muscle compared to CT μ-maps. The study emphasizes the need for rigorous validation of attenuation correction methods in complex anatomical regions for accurate treatment delivery and improved patient care in PET/MR and radiotherapy. Future research should focus on refining and validating μ-map generation algorithms for improved accuracy in both MR-based and pseudo-CT methods, especially in complex anatomical regions. Exploring novel approaches like deep learning for tissue segmentation could enhance reliability. Longitudinal studies assessing the clinical impact of μ-map discrepancies on treatment outcomes are crucial, as is interdisciplinary collaboration to optimize techniques and translate findings into clinical practice effectively

Acknowledgment

The authors would like to express sincere gratitude to St. Olav’s Hospital, Trondheim, specifically the Cancer Clinic and Clinic of Radiology and Nuclear Medicine, for their valuable support and collaboration during the course of this research. Appreciation is also extended to the Department of Medical Physics at the University of Ghana and the NORPART Project, facilitating the Ghana-Norway Collaboration in Medical Physics and Radiography Education. This collaborative effort has significantly enriched the study's outcomes, and the authors acknowledge the crucial role played by these institutions in advancing research endeavors.

References

1. Teimoorisichani M, Panin V, Rothfuss H, Sari H, Rominger A, Conti M. A CT-less approach to quantitative PET imaging using the LSO intrinsic radiation for long-axial FOV PET scanners. Medical physics. 2022;49(1):309-23.
2. Schwenck J, Sonanini D, Cotton JM, Rammensee H-G, la Fougère C, Zender L. Advances in PET imaging of cancer. Nature Reviews Cancer. 2023;23(7):474-90.

3. Stefano A. Challenges and limitations in applying radiomics to PET imaging: possible opportunities and avenues for research. Computers in Biology and Medicine. 2024;179:108827.
4. Balogh V, MacAskill MG, Hadoke PW, Gray GA, Tavares AA. Positron emission tomography techniques to measure active inflammation, fibrosis and angiogenesis: potential for non-invasive imaging of hypertensive heart failure. Frontiers in Cardiovascular Medicine. 2021;8:719031.
5. Crișan G, Moldovean-Cioroianu NS, Timaru D-G, Andrieș G, Căinap C, et al. Radiopharmaceuticals for PET and SPECT imaging: a literature review over the last decade. International journal of molecular sciences. 2022;23(9):5023.
6. Windows-Yule C, Herald M, Nicuşan A, Wiggins C, Pratx G, Manger S. Recent advances in positron emission particle tracking: a comparative review. Reports on progress in physics. 2022;85(1):016101.
7. Shahi A. Evaluation of multi-angle imaging with planar organ-targeted positron emission tomography detectors 2024.
8. Massari R, Mok GS. New trends in single photon emission computed tomography (SPECT). Frontiers Media SA; 2023. p. 1349877.
9. Galldiks N, Kaufmann TJ, Vollmuth P, Lohmann P, Smits M, Veronesi MC. Challenges, limitations, and pitfalls of PET and advanced MRI in patients with brain tumors: A report of the PET/RANO group. Neuro-oncology. 2024:noae049.
10. Hussain S, Mubeen I, Ullah N, Shah SSUD, Khan BA, Zahoor M. Modern diagnostic imaging technique applications and risk factors in the medical field: a review. BioMed research international. 2022;2022(1):5164970.
11. Illimoottil M, Ginat D. Recent advances in deep learning and medical imaging for head and neck cancer treatment: MRI, CT, and PET scans. Cancers. 2023;15(13):3267.
12. Cabello J, Lukas M, Förster S, Pyka T, Nekolla SG, Ziegler SI. MR-based attenuation correction using ultrashort-echo-time pulse sequences in dementia patients. Journal of Nuclear Medicine. 2015;56(3):423-9.
13. Commandeur F, Simon A, Mathieu R, Nassef M, Arango JDO, Rolland Y. MRI to CT prostate registration for improved targeting in cancer external beam radiotherapy. IEEE journal of biomedical and health informatics. 2016;21(4):1015-26.
14. Dowling JA, Sun J, Pichler P, Rivest-Hénault D, Ghose S, Richardson H. Automatic substitute computed tomography generation and contouring for magnetic resonance imaging (MRI)-alone external beam radiation therapy from standard MRI sequences. International Journal of Radiation Oncology* Biology* Physics. 2015;93(5):1144-53.
15. Edmund JM, Nyholm T. A review of substitute CT generation for MRI-only radiation therapy. Radiation Oncology. 2017;12:1-15.
16. Johansson A, Karlsson M, Yu J, Asklund T, Nyholm T. Voxel-wise uncertainty in CT substitute derived from MRI. Medical physics. 2012;39(6Part1):3283-90.
17. Decazes P, Hinault P, Veresezan O, Thureau S, Gouel P, Vera P. Trimodality PET/CT/MRI and radiotherapy: a mini-review. Frontiers in oncology. 2021;10:614008.
18. Pozaruk A, Pawar K, Li S, Carey A, Cheng J, Sudarshan VP. Augmented deep learning model for improved quantitative accuracy of MR-based PET attenuation correction in PSMA PET-MRI prostate imaging. European journal of nuclear
19. Lee JS. A review of deep-learning-based approaches for attenuation correction in positron emission tomography. IEEE Transactions on Radiation and Plasma Medical Sciences. 2020;5(2):160-84.
20. Shandiz MS, Rad HS, Ghafarian P, Karam MB, Akbarzadeh A, Ay MR. MR-guided attenuation map for prostate PET-MRI: an intensity and morphologic-based segmentation approach for generating a five-class attenuation map in pelvic region. Annals of nuclear medicine. 2017;31:29-39.
21. Slates RB, Farahani K, Shao Y, Marsden PK, Taylor J, Summers PE. A study of artefacts in simultaneous PET and MR imaging using a prototype MR compatible PET scanner. Physics in Medicine & Biology. 1999;44(8):2015.
22. Marshall H, Stodilka R, Theberge J, Deans, L, Sykes, .JM, et al. A comparison of MR-based attenuation correction in PET versus SPECT. Physics in Medicine & Biology. 2011;56(14):4613.
23. Dowling JA, Lambert J, Parker J, Salvado O, Fripp J, Capp A. An atlas-based electron density mapping method for magnetic resonance imaging (MRI)-alone treatment planning and adaptive MRI-based prostate radiation therapy. International Journal of Radiation Oncology* Biology* Physics. 2012;83(1):e5-e11.
24. Fuchs J, Neuberger T, Rolletschek H, Schiebold S, Nguyen TH, Borisjuk N. A noninvasive platform for imaging and quantifying oil storage in submillimeter tobacco seed. Plant physiology. 2013;161(2):583-93.
25. Hofmann M, Steinke F, Scheel V, Charpiat G, Farquhar J, Aschoff P. MRI-based attenuation correction for PET/MRI: a novel approach combining pattern recognition and atlas registration. Journal of nuclear medicine. 2008;49(11):1875-83.
26. Carney JP, Townsend DW, Rappoport V, Bendriem B. Method for transforming CT images for attenuation correction in PET/CT imaging. Medical physics. 2006;33(4):976-83.
27. Wagenknecht G, Kaiser H-J, Mottaghy FM, Herzog H. MRI for attenuation correction in PET: methods and challenges. Magnetic resonance materials in physics, biology and medicine. 2013;26:99-113.
28. Arabi H, Zaidi H. Magnetic resonance imaging-guided attenuation correction in whole-body PET/MRI using a sorted atlas approach. Medical image analysis. 2016;31:1-15.
29. Aasheim LB, Karlberg A, Goa PE, Håberg A, Sørhaug S, Fagerli U-M. PET/MR brain imaging: evaluation of clinical UTE-based attenuation correction. European journal of nuclear medicine and molecular imaging. 2015;42:1439-46.
30. Siversson C, Nordström F, Nilsson T, Nyholm T, Jonsson J, Gunnlaugsson A. MRI only prostate radiotherapy planning using the statistical decomposition algorithm. Medical physics. 2015;42(10):6090-7.
31. Florkow MC, Willemsen K, Mascarenhas VV, Oei EH, van Stralen M, Seevinck PR. Magnetic resonance imaging versus computed tomography for Three-Dimensional bone imaging of musculoskeletal

pathologies: a review. Journal of Magnetic Resonance Imaging. 2022;56(1):11-34.
32. Lee TC, Alessio AM, Miyaoka RM, Kinahan PE. Morphology supporting function: attenuation correction for SPECT/CT, PET/CT, and PET/MR imaging. The quarterly journal of nuclear medicine and molecular imaging: official publication of the Italian Association of Nuclear Medicine (AIMN)[and] the International Association of Radiopharmacology (IAR),[and] Section of the Society of. 2015;60(1):25.